CHAPTER 12
Cardiac Image Analysis: Motion and Deformation

Xenophon Papademetris
Yale University

James S. Duncan
Yale University

Contents

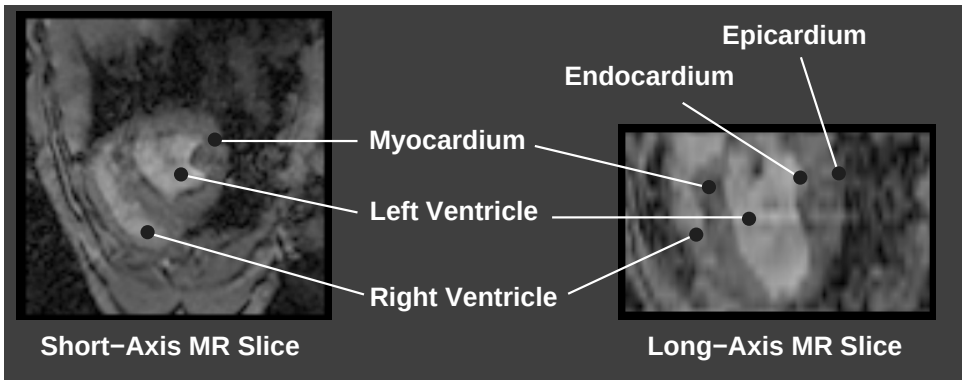

Figure 12.1: Geometry of the mammalian heart. In the discussion to follow, the terms endocardium and epicardium will be used to refer to the bounding surfaces of the left ventricular myocardium.

In this chapter, we describe research in the area of estimation of cardiac motion and deformation from medical images. We focus primarily on the use of 3D magnetic resonance image sequences, but we will also discuss the application of some methods to ultrafast CT and 3D echo.

12.1 Introduction

The estimation of cardiac motion and deformation from 3D images has been an area of major concentration in the medical image analysis. In these problems, the image data utilized are typically acquired in 16 frames consisting of 10 to 16 slices each. One such image slice through a canine heart acquired using magnetic resonance imaging is shown in Fig. 12.1 (as well as a reconstructed long-axis slice). In the figure, we label major areas such as the left and right ventricles and the two ventricular walls that bound the left ventricular myocardium (the endocardium and the epicardium). Most researchers have focused almost exclusively on the motion and deformation of the left ventricle. More recently, however, some preliminary work on right ventricular deformation has also appeared in the literature [1].

The estimation of regional 3D cardiac deformation is an important issue, as ischemic heart disease is a major clinical problem. Myocardial injury caused by ischemic heart disease is often regional. It is the fundamental goal of many types of cardiac imaging and image analysis to measure the regional function of the left ventricle (LV) in an effort to isolate the location and extent of ischemic or infarcted myocardium. Figure 12.2 illustrates the effect of a blocked artery; in this case, the left-anterior descending artery (LAD) has been occluded. There is a change in the deformation in a local region that is supplied by the LAD; instead of the normal thickening behavior, it actually thins on contraction. Quantitative estimation of

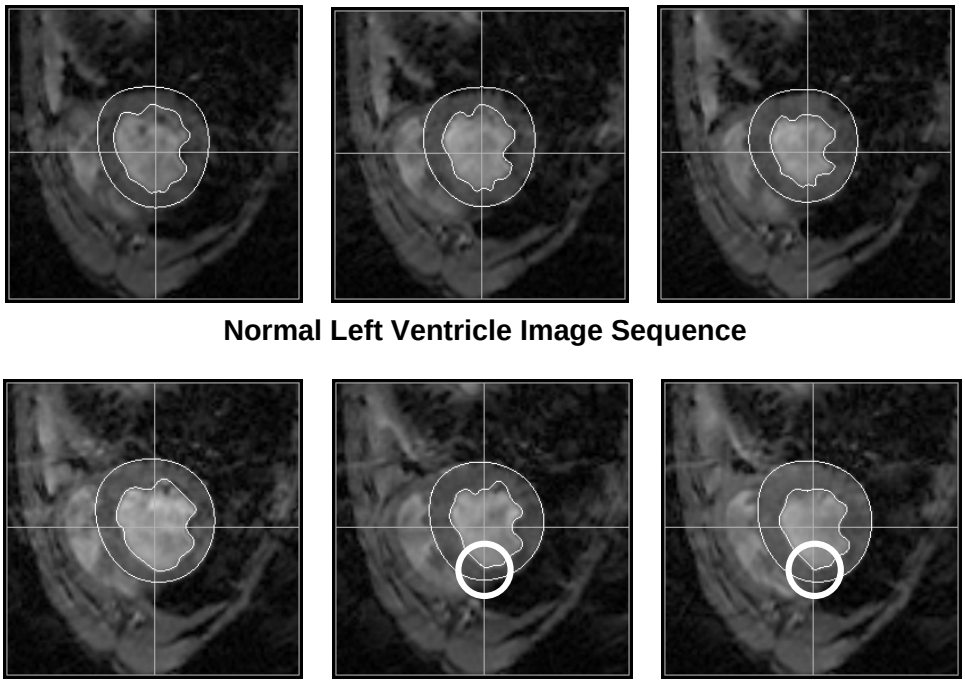

Figure 12.2: Short-axis magnetic resonance images from two 3D acquisitions of a canine heart. The top sequence was acquired before left coronary anterior artery occlusion and the bottom sequence postocclusion. The occlusion generates a disruption of the normal thickening behavior of the myocardium in contraction in the highlighted region. The quantification of such parameters from 3D image sequences is the focus of the methods reviewed in this chapter.

these changes is a major goal of cardiac image analysis, as it will hopefully allow for the measurement of both the location and the extent of the affected region.

In addition, the current management of acute ischemic heart disease is directed at establishing coronary reperfusion and, in turn, myocardial salvage. Also, understanding the physiology of the heart is an important focus of research in cardiology, for the evaluation of various surgical procedures such as transmyocardial revascularization [2].

The rest of this chapter reads as follows: In Section 12.2, we briefly describe alternative techniques for estimating cardiac deformation. These tend to be invasive and involve surgically implanted beads or ultrasound transducers. Then, in Sections 12.3 and 12.4, we turn our attention to current and previous research efforts in the medical imaging community with respect to estimating cardiac motion and defor-

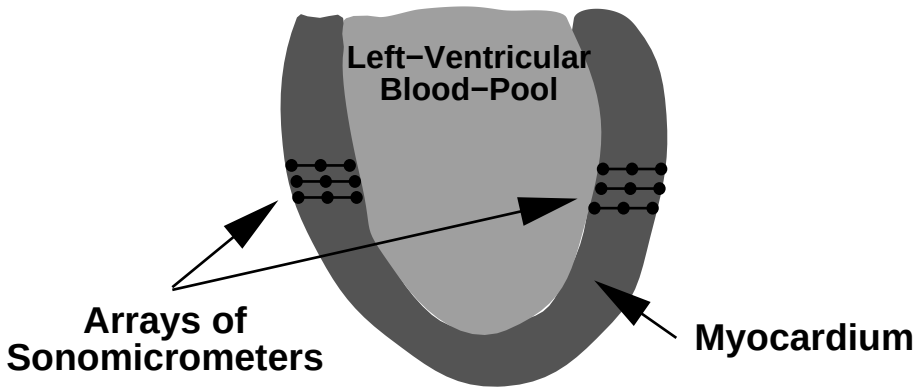

Figure 12.3: Typical placement of arrays of sonomicrometer crystal (or implanted bead) arrays in the left ventricle. These can produce highly accurate estimates of the deformation at a small number of locations in the left ventricle.

mation. Typically, any given method will combine a set of sparse, noisy, image-derived and sometimes partial set of displacement estimates (the "data") with a model which is used to simultaneously smooth and interpolate these estimates as necessary (the "model"). This combination of "data" and "model" produces the resulting displacement field. We will first analyze the "data" component of the presented methods in Section 12.3 and the "model" component in Section 12.4. In Section 12.5, we present in more detail one method, in attempt to illustrate better the more general descriptions of Sections 12.3 and 12.4. Then, in Section 12.6 we turn to the all important topic of validation. Finally, in Section 12.7 we present some possible future research directions in this area.

12.2 Invasive approaches to measuring myocardial deformation

A variety of work is evident in the cardiac physiology literature that attempts to quantitatively measure transmural myocardial strain. Several noteworthy efforts in particular have used sonomicrometers [3–5] and arrays of implanted markers (see, e.g., [6, 7]). For example, Fig. 12.3 shows a schematic of a typical implantation of sonomicrometers in the left ventricle. While accepted as being accurate, in both cases only a sparse number of specific sites on the LV can be measured, due to the difficulty in implanting the sonomicrometers and markers. It would be quite difficult to measure a large number of sites simultaneously.

Also, it is possible that these implanted devices can alter myocardial perfusion and function, although there is little published evidence of this. While many of these measurements are performed in animals, we note that some interesting measurements of strain using markers have been produced even in humans [8]. Finally, we also note that some researchers have looked at measuring *in vivo* strain using

attached strain gauges [9] (as noted in [10]), although little has been pursued along these lines.

12.3 Approaches to obtaining estimates of cardiac deformation from 4D images

There are two aspects to this problem; the first relates to the manipulation of the acquisition parameters in order to obtain the most-useful images, and the second to the postprocessing of these images for estimation of cardiac deformation. Regarding the first aspect, a significant level of activity has been performed within the magnetic resonance imaging (MRI) community regarding the development of MR tagging, and to a lesser extent, MR phase velocity imaging. The underlying physics of these techniques is beyond the scope of this chapter; the interested reader is referred to a review article by Leon Axel [11].

The second aspect of this problem, the analysis of the images, relates to work traditionally done in the computer vision community, especially in the areas of nonrigid motion estimation, including the case of variable illumination, segmentation, and surface mapping. A general, although somewhat dated coverage of the field can be found in Horn [12].

In this section, we focus on the image-derived characteristics used to obtain the initial, somewhat sparse, often noisy and partial displacements and/or velocities that are combined with a model to produce complete and dense displacement and deformation estimates.

12.3.1 Methods relying on magnetic resonance tagging

In this approach, grid lines at certain positions can be generated at one point in the cardiac cycle and their deformation tracked over a portion of the cycle, primarily using gated acquisition techniques. The development of the grid tagging approach to the measurement of myocardial strain has been vigorously pursued by two groups in particular — at the University of Pennsylvania [11] and Johns Hopkins [13] — who are the original developers of the tagging ideas. Figure 12.4 shows an example of such an acquisition. Three frames are shown; in frame 1, the original tags are laid out parallel to the vertical axis, and they are shown to deform with the material in the subsequent frames.

Much of these groups' current efforts are focused on how to create dense fields of measurements in 3D by putting together several orthogonal tagging grid acquisitions. Their approaches certainly show promise, because of the inherent capability of including discernible patterns that deform with the tissue, but they currently have the following limitations: (a) it is difficult to track the tags over the complete LV cycle, due to decay of the tags with time; (b) multiple acquisitions are required to assemble 3D information; and (c) it is still quite difficult to assemble the detected tags into a robust 3D analysis/display. All of these problems are being pursued aggressively by the two primary groups mentioned above, as well as by a few other

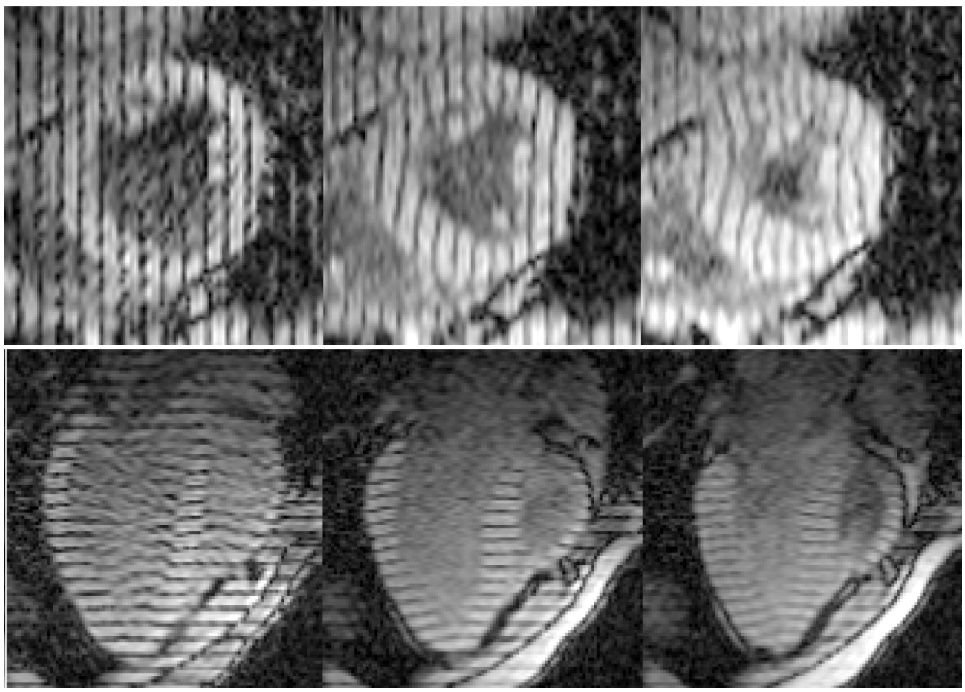

Figure 12.4: Samples of short-axis (top) and long-axis (bottom) magnetic resonance images illustrating magnetic resonance tagging at three time points in the cardiac cycle. Courtesy of Jerry L. Prince, John Hopkins University.

institutions (e.g. [14]).

In general, there seem to be three different approaches to estimating initial displacement data from magnetic resonance tagging as follows:

- Tagging in multiple intersecting planes and using the tag intersections as tokens for tracking (e.g. [14–16]).
- Tagging in multiple intersecting planes, and then for each tagging plane estimating the normal direction of motion perpendicular to the plane. This generates a sense of partial displacements (i.e., the component parallel to the tag lines is missing) to be combined later (e.g. [1, 17]).
- Attempting to model the tag fading over time using a model for the Bloch equations and using a variable-brightness optical flow approach to extract the displacements (e.g. [18, 19]).

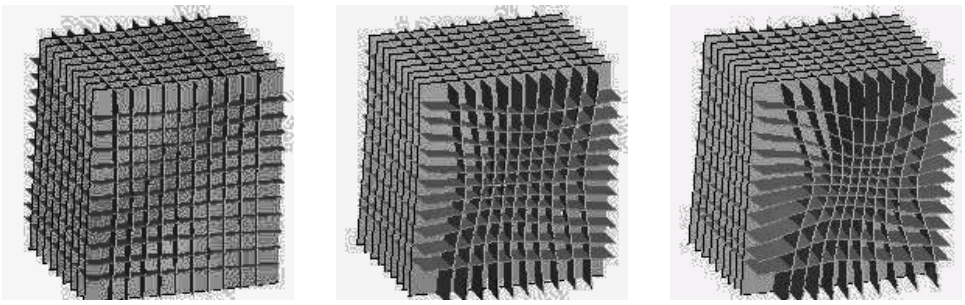

Figure 12.5: Reconstruction of three perpendicular tagging planes acquired in different acquisitions. From Kerwin et al. [15], Courtesy of Jerry L. Prince, John Hopkins University.

Using intersections. The multiple intersecting planes are either generated by imposing a tag-grid pattern in a single acquisition, which can be done only for two-dimensional grid patterns, or by tagging along different planes in separate acquisitions and superimposing the tagged planes to create the grid later (see work by Kerwin and Prince [15], Amini [14], Young and Axel [16], etc.) An example of the later approach is shown in Fig. 12.5, from the work of Kerwin and Prince [15]. The underlying idea is to try to generate "material"-markers at the intersection points, and then use these as the features for the overall motion-estimation scheme.

Using the whole tag lines. The second approach, rather than using just the intersections, tries to use the whole of the tag lines (planes). (See work by Haber and Metaxas [1], or Denney and Prince [17].) This has the advantage of being more robust to noise than the first approach, as it uses more of the tag line and can also provide partial information in regions where there are few intersections. This becomes especially useful in the case of the right ventricle [1], where the thickness of the heart wall is much smaller and the likelihood of having regularly spaced intersections is very low. The penalty paid for this is that, at this original stage, one can generate only displacement estimates perpendicular to the tag plane, which will need to be processed later in order to generate a full displacement field.

In both of the above approaches, in the preprocessing stage, there is also a need to identify which of the intersections or parts of the tag lines lie within the myocardium and then to discard all of the others. This results in the need for at least a crude segmentation of the myocardium; this is commonly done interactively, such as in the work of Guttman et al. [20], Young et al. [16] or Kumar et al. [21]. (It is worth noting, however, that Denney [22] proposes a new method that bypasses this segmentation step.)

Both the tag detection step and the presegmentation work, in general, use methods based on deformable models, following the original work by Kass [23]. (See

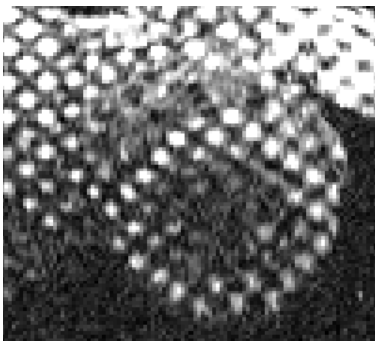

Figure 12.6: An example of a low-frequency tagged MRI image. From Thetokis and Prince [26]. Courtesy of Jerry L. Prince, John Hopkins University.

also chapter 3 and the review article by McInerney and Terzopoulos [24].) A deformable model tries to find the curve that minimizes an energy functional that consists of an image-based term (typically the gradient) and an internal energy or smoothness term. In the formulation of [23], it had the form

$$\int_s |\nabla I(x,y)|^2 + \alpha \left[\left(\frac{dx}{ds} \right)^2 + \left(\frac{dy}{ds} \right)^2 \right] + \beta \left[\left(\frac{d^2x}{ds^2} \right)^2 + \left(\frac{d^2y}{ds^2} \right)^2 \right] ds \,, \tag{12.1}$$

where $I(x,y)$ is the image as a function of the coordinates x, y; s is the arclength that parameterizes the curve; and α and β are the smoothing parameters. The gradient term ensures adherence to the image data, whereas the second term tries to keep the curve smooth. This approach is modified to allow for different deformable model geometries, such as grids [21], and for better image adherence terms using some knowledge of the underlying physics, such as in the case of [25].

Variable-brightness optical flow methods. In the third case, the whole image is used, and data are extracted using a variable-brightness optical flow approach on the image intensity. Sinusoidal tagging patterns are primarily used in this case, which provide for the smooth intensity fields needed for efficient optical flow computation. See Fig. 12.6 for an example of this.

The variable-brightness part of the algorithm is based on modeling the fading of the tag intensity over time using a model of the imaging process as generated by the Bloch equations [18, 19]. For example, in the work of Gupta [19], the signal (brightness) at time t is modeled as

$$\psi(t) = D_0 e^{-T_E/T_2}\left(1 - e^{-T_R/T_1}\right) + D_0 e^{-T_E/T_2}\,(\xi - 1)\left(e^{-t/T1} - e^{T_R - T_1}\right), \tag{12.2}$$

where D_0 is the proton density, T_1 and T_2 are the relation time constants, T_R is the repetition time, T_E is the echo time, and ξ is the tag modulation coefficient. The first three parameters (D_0, T_1, T_2) are properties of the underlying tissue, whereas the last three (T_R, T_E, ξ) are the acquisition parameters. In [19], a composite of the tissue parameters is estimated as part of the displacement estimation algorithm.

As with all intensity-based methods, the original estimates of the displacement field consist of the component of the displacements perpendicular to the isophotes, (this limitation is known as the aperture problem; see Horn [12] for details) which are later regularized to produce a full displacement estimate. The quality of these estimates are highest in the middle of the wall and can be very noisy near the myocardial boundaries. This method has the advantage of not having to detect tags explicitly, but here the brightness variation parameters must be either known or estimated. A rough presegmentation of the ventricle is also needed here, to avoid smoothing across the boundaries. These methods have, to the best knowledge of the authors, been applied only in 2D.

12.3.2 Methods relying on phase contrast MRI

Several investigators have employed changes in phase due to motion of tissue within a fixed voxel or volume of interest to assist in estimating instantaneous, localized velocities, and ultimately cardiac motion and deformation. While the basic ideas were first suggested by van Dijk [27] and Nayler [28], it was Pelc and his team [29–31] who first bridged the technique to conventional cine MR imaging and permitted the tracking of myocardial motion throughout the cardiac cycle. This technique relies basically on the fact that a uniform motion of tissue in the presence of a magnetic field gradient produces a change in the MR signal phase that is proportional to velocity. In principle, these instantaneous Eulerian velocities can be derived from each pixel in an image acquisition. An example of such an acquisition is shown in Fig. 12.7.

However, clusters of pixels within regions of interest (ROIs) are typically analyzed when predicting point-wise motion, primarily due to signal-to-noise issues. It is worth noting that, as with MR tagging, accurately tracking myocardial motion in 3D requires additional image processing, and little has been reported in the literature about this problem. Assembling the dense field phase velocity information into a complete and accurate 3D myocardial deformation map is currently a limiting problem for this technology. Furthermore, current phase-contrast velocity estimates near the endocardial and epicardial boundaries are less accurate. This is due to the fact that the required size of an ROI — for signal-to-noise purposes — is typically large and can include information from outside the myocardial wall.

Thus, as with MR tagging, the most accurate LV function information is obtained from the middle of the myocardial wall, and the least accurate information is usually near the endocardial and epicardial wall boundaries. In general, there seem to be the following two common approaches to extracting useful information from phase-contrast images:

- Processing the data directly to estimate strain rate tensors, e.g., [29, 32].
- Integrating the velocities over time, via some form of tracking mechanism to estimate displacements e.g., [33–36].

We also note that Shi [37] combined the phase-contrast velocities with shape-based displacements [38] within an integrated framework that is based on continuum mechanics.

12.3.3 Computer-vision-based methods

Quantifying the deformation of the LV can be seen as a two-step process: first, establish correspondence between certain points on the LV at time t and time $t+1$; and second, using these correspondences as a guide, solve for a complete mapping (embedding) of the LV between any two time frames. This problem can be posed for the entire myocardium or just portions of it, such as the endocardial surface alone. There has been considerable effort, in general, on these two topics, although rarely have they been addressed together.

One common approach to establishing correspondence is to track shaperelated features on the LV over time as reported by Goldgof [39], Ayache [40], McEachen [41], and Shi [38]. An example of such an approach in 2D is shown in Fig. 12.8. The preliminary displacement estimates here are, in general, generated using the following steps:

- Extract the endocardial and epicardial surfaces from the images.
- Calculate the quantity that is used as the shape feature from these surfaces. These tend to be the curvatures; either the principal curvatures as in [38] or the Gaussian curvature [39].
- Track points on the surfaces from one frame to the next by minimizing a metric such as bending energy or difference in curvature.

Then, the displacement field is smoothed (as was the case with previous methods) to produce the final output displacements. A validation study of shape-based tracking by comparing trajectories with implanted markers was reported by Shi et al. in [38], who found that the accuracy of tracking was within the resolution of the image voxel sizes. Another interesting approach by Tagare [42] poses the mapping problem in 2D as a bimorphism between two curves, thus eliminating the basic asymmetry in the tracking process. This has not been extended to 3D yet.

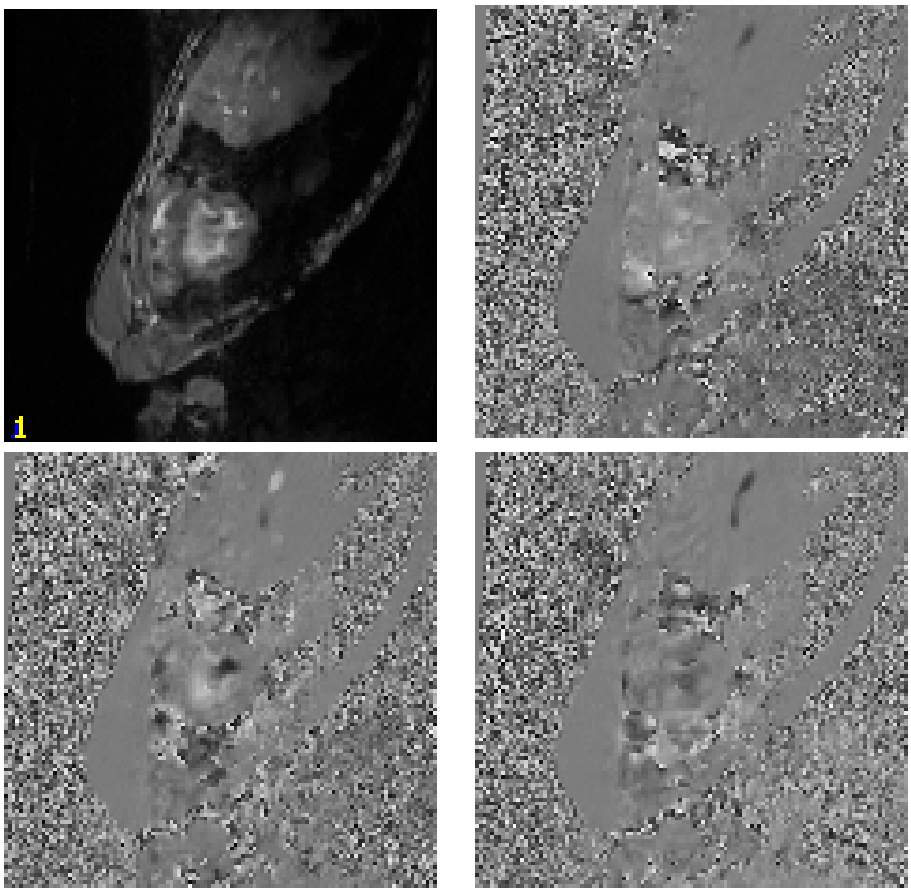

Figure 12.7: One slice from a volumetric dataset obtained using magnetic resonance phase contrast. The magnitude image is shown in the top left image. The other images show the magnitudes of the velocity in the X, Y, and Z directions, respectively.

In general, all of the methods here depend on an accurate segmentation of the LV walls, but have the advantage of being imaging modality independent. They have been used on MR, CT [38], and 3D ultrasound [43]. The dependency on obtaining an accurate segmentation, however, remains a significant issue, as there still are no fully automated robust and efficient LV surface segmentation methods. The accuracy of the LV segmentation needed for these methods to be successful is obviously greater than in the case of methods using MR tagging. This is because the surfaces themselves provide the features, as opposed to being bounding surfaces within which to search for intersections. We will examine a shape-tracking approach in more detail, in the case study in Section 12.5.

There has been some work done on using the intensity of the images directly

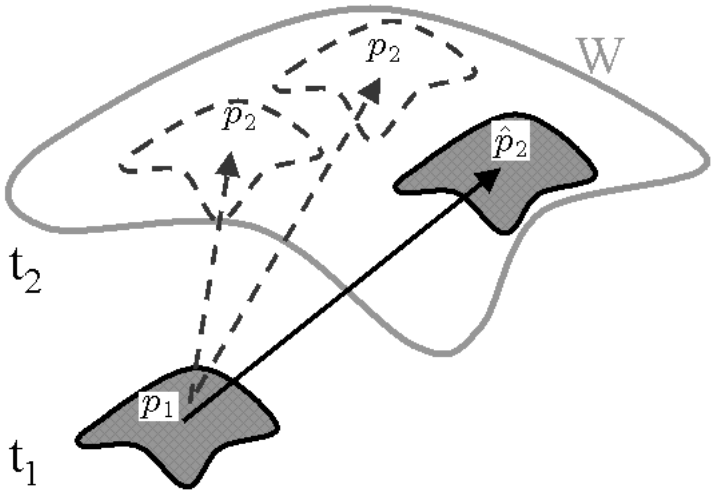

Figure 12.8: Example of the shape-tracking approach. The goal is to map the original surface to the final surface. For a point p_1 on the original surface, a window W of plausible matching points on the final surface is generated. Then, the point p_2 in W that has the most similar shape properties to p_1 is selected as the candidate match point. The distance function for shape similarity is typically based on the curvature(s).

to track the LV. Song and Leahy [44] used the intensity in ultrafast CT images to calculate the displacement fields for a beating heart. This is similar in scope to some of the work done with MR tagging (e.g., [19]), but it does not have the advantage of a specially modulated image.

12.4 Modeling used for interpolation and smoothing

In general, the initial displacement fields produced by the methods discussed in the previous section have the following characteristics:

- They are *sparse*. Displacements and/or velocities are only available at certain points and not for the whole of the myocardium.
- They are *noise corrupted*. This is an inherent problem in all medical image analysis methods, although the level of noise is very method dependent.
- They may be *partial*. Even where displacements and/or velocities are available, only a certain component of the displacement vector may be known.

The estimation of accurate myocardial deformation requires a dense, smooth, and complete displacement field. This is because the deformation is typically captured in terms of the strain that is a function of the derivatives of the displacement

field. The process of taking derivatives is very noise sensitive, and this is what makes this problem so challenging as compared to simply estimating the volume of the LV which is an integral measure and hence relatively less sensitive to noise.

The interpolation and smoothing of the displacement field has been attacked in a number of ways. This step essentially constitutes the modeling step, and it is data-independent. The models contain implicitly or explicitly the assumptions made about the displacement field. All of the "models" currently used in this area are passive; they ignore the fact that the heart is an actively contracting organ and not a passive lump of tissue. Some of the modeling strategies are

- Impose a regularization constraint that penalizes the spatial derivatives, either explicitly, as in [17, 19, 45], or combined in some cases with an isochoric constraint[1] [17,44]. This is further developed in the use of explicit continuum mechanics models, which behave as regularizers, as in [1, 38, 46].
- Model the displacement field by using a smooth spatial parameterization such as affine [33, 47] or splines [14, 15]. This method is used most often when displacement field modeling and tag extraction are combined in a single step, and is driven by the ease of parameterizing the geometry.
- Use of temporal smoothness or damping [1, 37, 42, 48] and temporal periodicity constraints [41].

In a sense, all of the above methods try to penalize the derivatives of the displacement, either in space, time, or both. We note that imposing a polynomial distribution such as an affine model is equivalent to setting all derivatives higher than a certain order to zero. This is a limiting case of penalizing spatial derivatives.

Spatial smoothness constraints. The application of spatial smoothness constraints relies on the intuition that given that the myocardium is a single object, its displacement field can be expected to be smooth. If this is violated, then the tissue would tear apart. Therefore, high values of derivatives in the displacement field (or equivalently high frequency components of its Fourier transform in the spatial sense) are likely to be the result of noise. This results in methods that penalize the spatial derivatives, as in the optical flow method proposed by Horn and Schunk [49]. In this case, the optimal displacement field is found as a trade-off between satisfying the *gradient constraint equation* and a regularization term as follows:

$$\hat{u} = \underset{u}{\arg\min} \int_{\mathbf{x}} \left(\frac{dI}{dt} + u.\nabla I \right)^2 + \lambda \left[\sum_{ij} \left(\frac{du_i}{dx_j} \right)^2 \right] d\mathbf{x}\,, \tag{12.3}$$

[1]The myocardium is considered to be nearly incompressible and the isochoric constraint tries to enforce this incompressibility.

where the u is the displacement vector field over a space x that can be two- or three-dimensional, t is time, and I represents the image.

The gradient constraint term $(I_t + u.\nabla I)^2$ essentially tries to match points of equal intensity and is the *data* term, whereas the sum of squared derivatives multiplied by the smoothness factor λ constitutes the regularizing term. The regularizing term can be thought of as a *model* term, as it contains *no* image-related information. It captures the authors' prior belief in the properties of the displacement field.

This framework is used in many of the approaches described earlier, although it is adapted to either match the data or the prior information. For example, in the case of the variable-brightness optical flow method [18,19], the gradient constraint term is replaced by a different measure that allows for the fading in the tag pattern. In a more general case, the gradient constraint term can be replaced by an image-data adherence term. This term tries to find a displacement field that stays close to some pre-existing displacement estimates obtained by using approaches described in Section 12.3. For example, if an estimate u^m of the displacement field exists, we could modify the Horn and Schunk framework as follows:

$$\hat{u} = \underset{u}{\arg\min} \int_{\mathbf{x}} |u - u^m|^2 + \lambda \left[\sum_{ij} \left(\frac{du_i}{dx_j} \right)^2 \right] d\mathbf{x} \,. \tag{12.4}$$

We can expand on this model by also using an isochoric constraint that tries to penalize volume changes, as was done in [17,44]. This takes the form $(\nabla.u)^2$ and is motivated by the fact that the myocardium — like most soft tissue — is thought to be approximately incompressible[2]. Alternatives also include the use of thin-spline energy terms [15] or b-spline terms [14].

The combination of the smoothness and isochoric terms describes the myocardium in terms of what is essentially an internal energy function. Continuum mechanics models of the myocardium as found in the biomechanics literature [50] are also described as internal energy functions, which also essentially penalize derivatives. So, it is a natural step at this point to try to bring some of this knowledge into the inverse problem of motion estimation. To do this, the regularization term is replaced by an explicit mechanical model, which in most cases is an isotropic linear elastic [1, 37, 48] and in the case study we will consider it as transversely isotropic. This allows for us to account for the preferential stiffness of the myocardium along the fiber directions. It is interesting to note that, from continuum mechanics theory [51], an internal energy function can describe a real material if and only if it is invariant to rigid translation and rotation; otherwise, this material violates the second law of thermodynamics. It can be shown that the classical model of Horn and Schunk is *not* invariant to rotation and would fail this criterion. This is derived in the Appendix.

[2]There is in fact some change in volume, due to blood flow (reperfusion) into the wall, but this is considered to be small.

If we discretize Eq. (12.4), differentiate it with respect to u, and concatenate all the individual displacements u into a large vector U, we can write the generalized expression:

$$[K]U = F\,, \tag{12.5}$$

where K is the assembled matrix of local derivative operators (as in [23]) and is sparse. This contains the model constraints that can be derived either from a regularization term or an explicit continuum mechanics model. F is the external driving force that tries to deform the model to adhere to the image data. This equation is most easily solved using the finite element method [52] , in cases of complex geometry and especially in three dimensions.

Temporal smoothness constraints. There are two types of temporal smoothness constraints in the literature. In the first case, we have an explicit temporal filtering scheme applied to individual displacements. This is primarily, but not exclusively, done in the case where the input data is derived from phase contrast velocity. In the work of Meyer [33], a Kalman-filtering approach is used to smooth the displacement field. Zhu [35] and McEachen [41] parameterize the problem in the frequency domain by expanding the displacement of an individual point over time in terms of Fourier series and try to take advantage of the periodicity of the left-ventricular motion.

The second case involves extending Eq. (12.5) to include dynamics. This results in the following generalized expression:

$$M\ddot{U} + C\dot{U} + KU = F\,, \tag{12.6}$$

where M is a mass matrix and C is a damping matrix. This approach also results in a form of temporal smoothing, which is motivated by similar approaches in continuum mechanics. In the work of Park et al. [48], this was reduced to $C\dot{\mathbf{u}} = F$ by ignoring the mass matrix and setting the stiffness to 0. In [1], the stiffness term is also preserved. The full dynamical model is employed in Shi [37]; in this case, both shape-based displacements and phase-contrast velocity information are used. The full dynamical model is also used in work done in the computer vision and graphics communities by Metaxas and Terzopoulos [53].

We note that Pentland [54] and Nastar [55] also use this approach and, by ignoring the damping term, reduce it to a modal finite element equation, which parameterizes the deformation in terms of the eigenmodes of the stiffness matrix K. In both of these approaches, however, there is no explicit notion of correspondence between material points, and the displacements are found using a global distance measure.

12.5 Case study: 3D cardiac deformation

In order to further clarify the more general statements of the previous sections, in this section we describe one approach to estimating the regional deformation of the left ventricle from magnetic resonance images. It has been previously reported in [43, 46]. We use a biomechanical model to describe the myocardium and shape-based tracking displacement estimates on the epi- and endo cardial walls to generate the initial displacement estimates. These are integrated in a Bayesian estimation framework, and the overall problem is solved using the finite element method. This method produces *quantitative regional* 3D cardiac deformation estimates. We also show results from 3D ultrasound data that illustrates the versatility of this approach.

12.5.1 Obtaining initial displacement data

In this work, we used both magnetic resonance and ultrasound images that were acquired as follows:

MR images. ECG-gated magnetic resonance imaging was performed on a GE Signa 1.5 Tesla scanner. Axial images through the LV were obtained with the gradient echo cine technique. The imaging parameters were section thickness = 5 mm, no intersection gap, 40 cm field of view, TE 13 msec, TR 28 msec, flip angle 30°, flow compensation in the slice and read gradient directions, 256×128 matrix, and 2 excitations. The resulting 3D image set consists of 16 2D image slices per temporal frame, and 16 temporal 3D frames per cardiac cycle. The dogs were positioned in the magnetic resonance scanner for initial imaging under baseline conditions. The left anterior descending coronary artery was then occluded, creating an infarct region where there was mechanical disfunction, and a second set of images was acquired. An example of such an acquisition was shown in Fig. 12.2.

Ultrasound. The images were acquired using an HP Sonos 5500 Ultrasound System with a 3D transducer (Transthoracic OmniPlane 21349A (R5012)). The 3D probe was placed at the apex of the left ventricle of an open-chest dog using a small ultrasound gelpad (Aquaflex) as a standoff. Each acquisition consisted of 13 to 17 frames per cardiac cycle depending on the heart rate. The angular slice spacing was 5°, resulting in 36 image slices for each frame.

Image segmentation. The endo- and epicardial surfaces were extracted interactively using a software platform [56]. This platform was originally developed for MR image data and subsequently modified to allow for the different geometry and image characteristics of ultrasound. For the automated part of the segmentation, we used an integrated deformable boundary method on a slice-by-slice basis. The external energy function of the deformable contour consisted of the standard intensity term and, in the case of ultrasound images, a texture-based term similar to

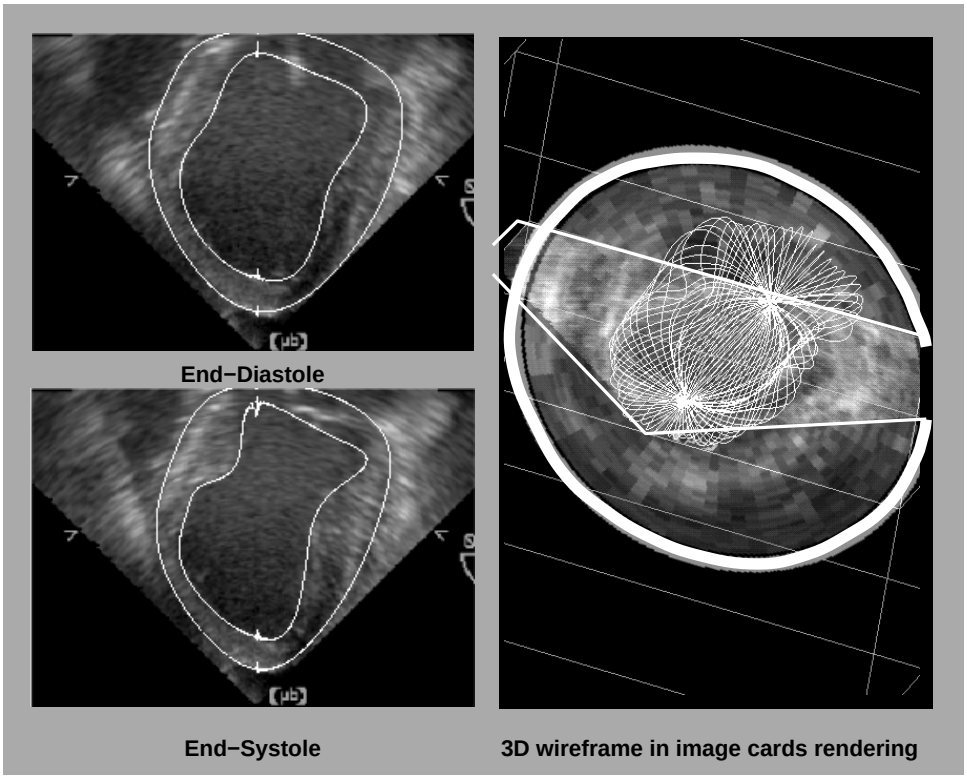

Figure 12.9: Ultrasound images and superimposed extracted contours. Only two of the eight frames are shown. The 3D rendering on the right shows all the wire-frame contours superimposed on a long axis (original) and a short-axis (interpolated) image slice.

the integrated method proposed in [57]; although in our case, the contours were parameterized as b-splines to allow for easy interaction.

Shape-tracking displacement estimates. In this work, the original displacements on the outer surfaces of the myocardium were obtained by using the shape-tracking algorithm for which details were presented in [38]. The method attempts to track points on successive surfaces using a shape similarity metric that tries to minimize the difference in principal curvatures, and was validated using implanted markers [38].

For example, consider point p_1 on a surface at time t_1, which is to be mapped to a point p_2 on the deformed surface at time t_2. First, a search is performed in a physically plausible region W_2 on the deformed surface, and the point $\hat{p}_2$ that has the local shape properties closest to those of p_1 is selected. The shape properties are captured in terms of the principal curvatures κ_1 and κ_2. The distance measure used is the bending energy required to bend a curved plate or surface patch to a

newly deformed state. This is labeled as d_{be} and is defined as

$$d_{be}(p1, p2) = A\left(\frac{[\kappa_1(p_1) - \kappa_1(p_2)]^2 + [\kappa_2(p_1) - \kappa_2(p_2)]^2}{2}\right). \tag{12.7}$$

The displacement estimate vector for each point p_1, u_1^m is given by

$$u_1^m = \hat{p}_2 - p_1 \quad , \quad \hat{p}_2 = \underset{p_2 \in W_2}{\arg\min}\left[d_{be}(p1, p2)\right].$$

Confidence measures in the match. The bending energy measurement for all of the points inside the search region W_2 are recorded as the basis for measuring the *strength* and *uniqueness* of the matching choices. The value of the minimum bending energy in the search region between the matched points indicates the goodness of the match. Denoting this value as m_g, we have the following measurement for matching goodness:

$$m_g(p_1) = d_{be}(p_1, \hat{p}_2). \tag{12.8}$$

On the other hand, it is desirable that the chosen matching point is a unique choice among the candidate points within the search window. Ideally, the bending energy value of the chosen point should be an outlier (much smaller value) compared to the values of the rest of the points. If we denote the mean value of the bending energy measures of all the points inside window W_2 except the chosen point as $\bar{d}_{be}$ and the standard deviation as σ_{be}^d, we define the uniqueness measure as

$$m_u(p_1) = \frac{d_{be}(p_1, \hat{p}_2)}{\bar{d}_{be} - \sigma_{be}^d}. \tag{12.9}$$

This uniqueness measure has a high value if the bending energy distance d_{be} to the chosen point is large compared to some reference value (mean minus standard deviation of the remaining bending energy measures). Combining these two measures together, we arrive at one *confidence measure* $c^m(p_1)$ for the matched point $\hat{p}_2$ of point p_1:

$$c^m(p_1) = \frac{1}{k_{1,g} + k_{2,g} m_g(p_1)} \times \frac{1}{k_{1,u} + k_{2,u} m_u(p_1)}, \tag{12.10}$$

where $k_{1,g}, k_{2,g}, k_{1,u}$, and $k_{2,u}$ are scaling constants for normalization purposes. We normalize the confidences to lie in the range 0 to 1.

Modeling the initial displacement estimates. Given a set of displacement vector measurements u^m and confidence measures c^m, we model these estimates probabilistically by assuming that the noise in the individual measurements is normally distributed with zero mean and a variance σ^2 equal to $\frac{1}{c^m}$. In addition, we assume

that the measurements are uncorrelated. Given these assumptions, we can write the measurement probability for each point as

$$p(u^m|u) = \frac{1}{\sqrt{2\pi\sigma^2}} e^{-\frac{(u-u^m)^2}{2\sigma^2}} . \tag{12.11}$$

12.5.2 Modeling the myocardium

The passive properties of the left-ventricular myocardium are captured using a biomechanical model. We use an anisotropic linear elastic model, which allows us to incorporate information about the preferential stiffness of the tissue along fiber directions from [58], which are shown in Fig. 12.10. The model is described in terms of an internal or strain energy function.

Definition of strain. Consider a body $B(0)$, which after time t moves and deforms to body $B(t)$. A point X on $B(0)$ goes to a point x on $B(t)$ and the transformation gradient F is defined as $dx = FdX$. The deformation is expressed in terms of the strain tensor ϵ. Because the deformations to be estimated in this work are larger than 5%, we use a finite strain formulation implemented using a logarithmic strain ϵ^L, which is defined as $\epsilon = ln\sqrt{F.F^t}$. Since the strain tensor is a 3×3 symmetric second-rank tensor (matrix), we can rewrite it in vector form as $e = [\epsilon_{11}\ \epsilon_{22}\ \epsilon_{33}\ \epsilon_{12}\ \epsilon_{13}\ \epsilon_{23}]^t$. This will enable us to express the tensor equations in a more familiar matrix notation.

Strain energy function. The mechanical model can be defined in terms of a strain energy function. The simplest useful continuum model in solid mechanics is the linear elastic one that is of the form $W(C,u) = e(u)^t Ce(u)$, where C is a 6×6 matrix and defines the material properties of the deforming body, and $e(u)$ is the strain vector that is a function of the displacement. The left ventricle of the heart is specifically modeled as a transversely elastic material to account for the preferential stiffness in the fiber direction, by using this matrix C:

$$C^{-1} = \begin{bmatrix} \frac{1}{E_p} & \frac{-\nu_p}{E_p} & \frac{-\nu_{fp}}{E_f} & 0 & 0 & 0 \\ \frac{-\nu_p}{E_p} & \frac{1}{E_p} & \frac{-\nu_{fp}}{E_f} & 0 & 0 & 0 \\ \frac{-\nu_{fp}E_f}{E_p} & \frac{-\nu_{fp}E_f}{E_p} & \frac{1}{E_f} & 0 & 0 & 0 \\ 0 & 0 & 0 & \frac{2(1+\nu_p)}{E_p} & 0 & 0 \\ 0 & 0 & 0 & 0 & \frac{1}{G_f} & 0 \\ 0 & 0 & 0 & 0 & 0 & \frac{1}{G_f} \end{bmatrix} , \tag{12.12}$$

where E_f is the fiber stiffness, E_p is cross-fiber stiffness, ν_{fp}, ν_p are the corresponding Poisson's ratios, and G_f is the shear modulus across fibers. ($G_f \approx E_f / (2(1+\nu_{fp}))$). If $E_f = E_p$ and $\nu_p = \nu_{fp}$, this model reduces to the more common isotropic linear elastic model. The fiber stiffness was set to be 3.5 times greater than the cross-fiber stiffness [58]. The Poisson's ratios were both set to 0.4 to model approximate incompressibility.

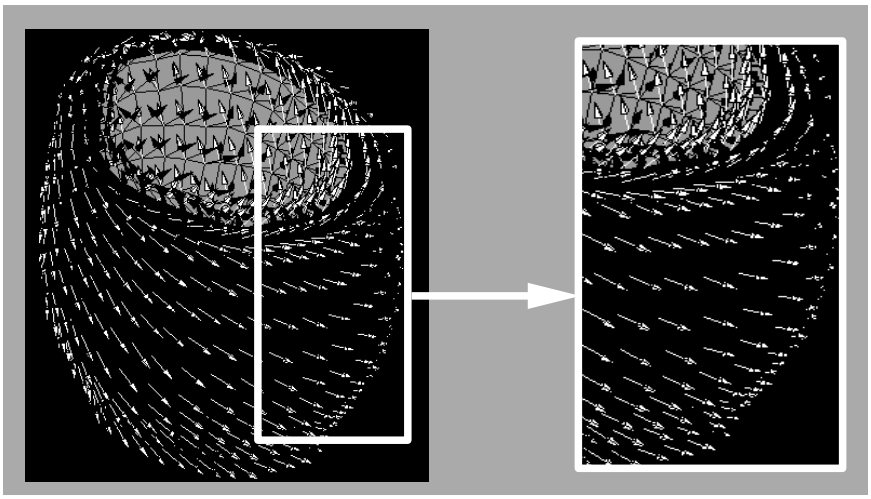

Figure 12.10: Fiber direction in the (canine) left ventricle as defined in Guccione et al. [58].

A probabilistic description of the model. As previously demonstrated by Christensen et al. [59], there is a correspondence between an internal energy function and a Gibbs prior. If the mechanical model is described in terms of an internal energy function $W(C,u)$, where C represents the material properties and u the displacement field, then we can write an equivalent prior probability density function $p(u)$ [see Eq. (12.14)] of the Gibbs form:

$$p(u) = k_1 \exp\left[-W(C,u)\right] . \tag{12.13}$$

12.5.3 Integrating the data and model terms

Having defined both the data term [Eq. (12.11)] and the model term [Eq. (12.13)] in terms of probability density functions, we naturally proceed to write the overall problem in a Bayesian estimation framework as follows: Given a set of noisy input displacement vectors u^m, the associated noise model $p(u^m|u)$ (data term), and a prior probability density function $p(u)$ (model term), find the best output displacements $\hat{u}$ that maximize the posterior probability $p(u|u^m)$. Using Bayes' rule we can write

$$\hat{u} = \underset{u}{\arg\max}\, p(u|u^m) = \underset{u}{\arg\max} \left[\frac{p(u^m|u)p(u)}{p(u^m)}\right] . \tag{12.14}$$

The prior probability of the measurements $p(u^m)$ is a constant once these measurements have been made and therefore drops out of the minimization process.

Taking logarithms in Eq. (12.14) and differentiating with respect to the displacement field u results in a system of partial differential equations. When discretized, this system of equations has the same form as Eq. (12.5), with the K matrix being a function of the mechanical model and the geometry and A a function of the data variances. This is solved using the finite element method [52]. The first step in the finite element method is the division or tessellation of the body of interest into elements; these are commonly tetrahedral or hexahedral in shape. Once this is done, the partial differential equations are written down in integral form for each element, and then the integral of these equations over all of the elements is taken to produce the final set of equations. For more information, one is referred to textbooks such as Bathe [52] . The final set of equations is then solved to produce the output set of displacements.

For each frame between end-systole (ES) and end-diastole (ED), a two-step problem is posed: (a) solving Eq. (12.14) and (b) using a modified nearest-neighbor technique to map the position of all points on the endo- and epicardial surfaces so they lie on the endo- and epicardial surfaces at the next frame, and solving Eq. (12.14) once more using this added constraint. This ensures that there is no bias in the estimation of the radial strain.

12.5.4 Results

In this section, we present results from the application of this methodology on multiple (16) sets of multiple time-frame sequences of *in vivo* left-ventricular MR images. These consisted of eight canine experiments where images were acquired before and after coronary occlusion. These will be referred to as the normal and postocclusion studies. We also present some more preliminary results from three canine experiments using ultrasound images. Of these, one was a normal study and the other two were postocclusion studies.

In both cases, the images were segmented interactively using [56] and the surfaces sampled to 0.5 voxel resolution, at which point curvatures were calculated and the shape-tracking algorithm was used to generate initial displacement estimates. The heart wall was divided into 1,000–2,000 hexahedral elements (depending on the geometry), and the anisotropic linear elastic model was used to regularize the displacements. The computational time after the segmentation was on the order of 2–4 hrs/dog (depending on the heart rate and hence the number of image frames) on a Silicon Graphics Octane with an R10000 195 MHz processor and 128 MB RAM.

For the purpose of analyzing the results, the left ventricle of the heart was divided into a number of cross-sectional slices depending on its size and the post mortem information to which it was compared. Slice 1 was located at the bottom or apex of the ventricle. Each slice was further subdivided into 4 or 8 sectors; an example is shown in Fig. 12.11.

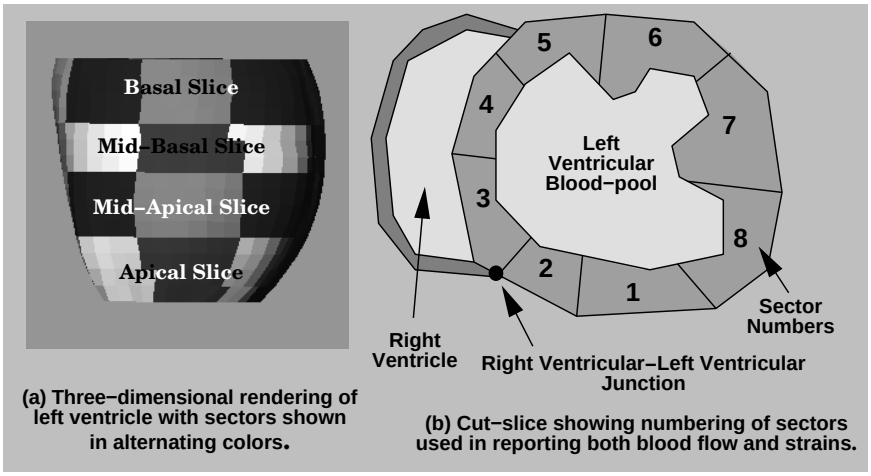

Figure 12.11: Typical division of the left ventricle into slices and sectors for the purpose of reporting results.

Normal MRI preocclusion results. For reporting purposes, the left ventricle was divided into three slices, each consisting of four sectors. We observed uniformity of radial (R) and circumferential (C) strains (ranges: $R = 15 \pm 6\%$ to $23 \pm 7\%$; $C = -9 \pm 5\%$ to $-12 \pm 2\%$). Regional LV strains and shears were consistent among dogs and comparable to values derived using both implanted markers and MR tagging [60]. An example of radial strain development is shown in Fig. 12.12.

Postocclusion MRI results. Here, the ventricle was divided to have the same number of slices as the original images, so as to correspond with postmortem histochemical staining maps of the actual injury zone. Each slice was further subdivided into eight sectors. The histochemical staining maps were used to label these sectors as one of four categories: infarcted (INF), mixed (MIX), adjacent (BD), and normal (NL). Given the relative uniformity of the radial and circumferential strains from the normal data set, we tested whether any of the strain components as estimated in the postocclusion studies could be used to discriminate between these different classes (INF, MIX, BD, NL). We found that the circumferential strain discriminated all myocardial regions to a level of significance < 0.05. This demonstrated that this methodology can be applied to discriminate different regions noninvasively. This is illustrated graphically in Fig. 12.13. An example of radial strain development in a postocclusion heart is shown in Fig. 12.14.

Ultrasound results. In two of the three studies, a coronary occlusion created an area of disfunction that we call the risk area. Regional blood flow in the heart wall was determined using a radio-labeled microsphere technique [61]. The blood-flow

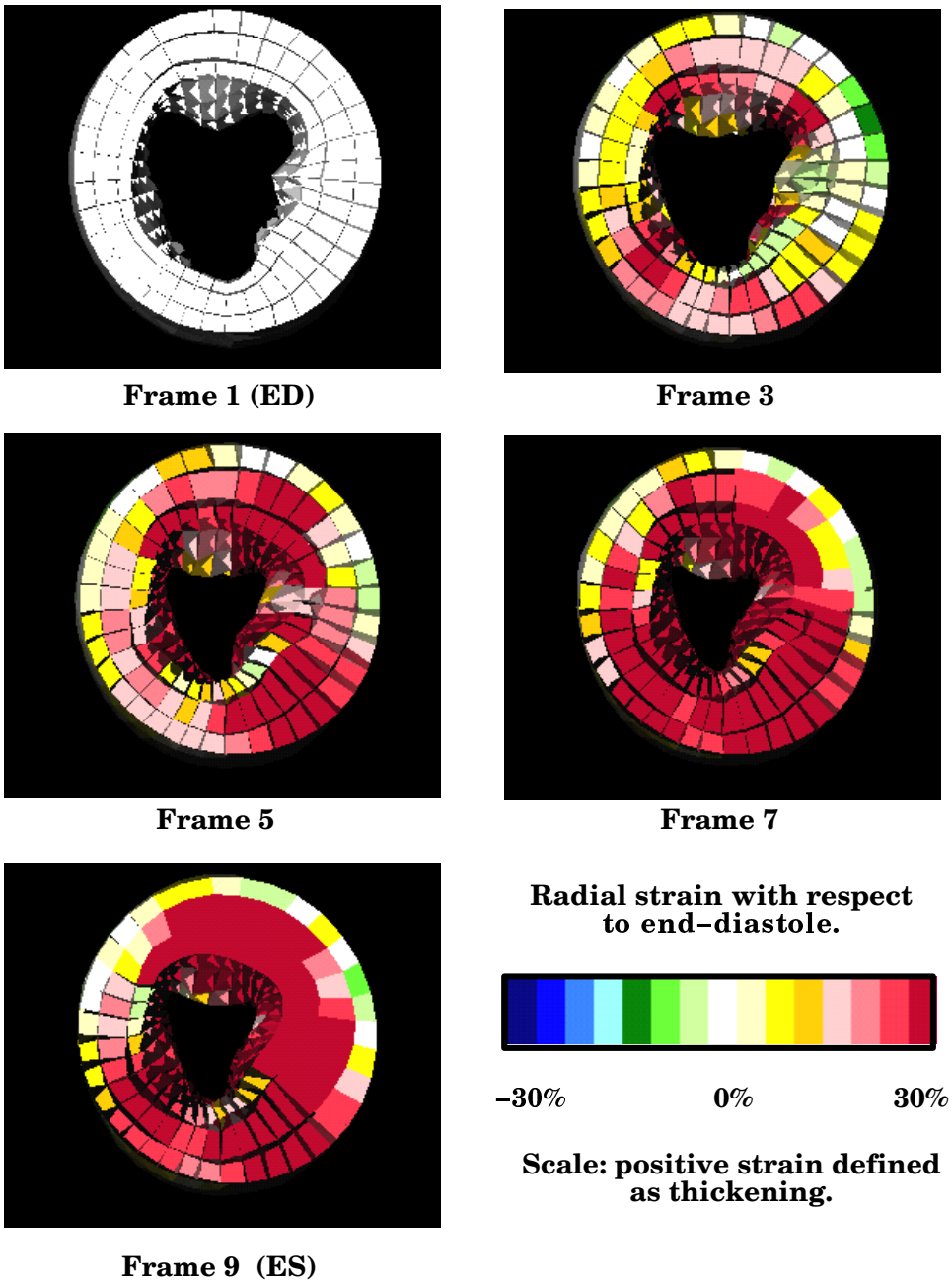

Figure 12.12: Radial strain development in a section of a normal left ventricle, as estimated from MRI data. Normal behavior is exhibited, which is thickening (red). The strain pattern is calculated throughout the left ventricle, but it is harder to visualize the full 3D picture, so a 2D cut is shown instead. (For a color version of this Figure see Plate 15 in the color section of this book.)

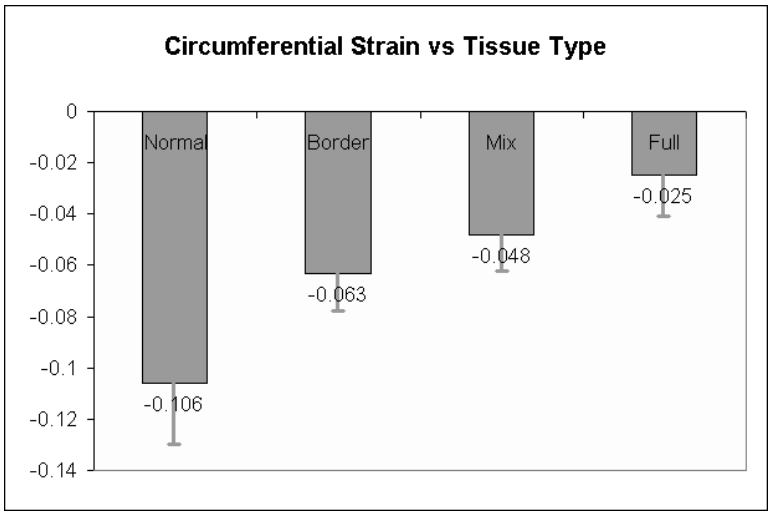

Figure 12.13: Plot showing average circumferential strain for different functional zones, as estimated from eight postocclusion MR data sets. The zones were identified using post-mortem information

measurements are used to identify the risk area and play no further role in this work. The heart was divided into four slices, and each slice was further subdivided into eight sectors, as shown in Fig. 12.11. A sector was labeled as being in the risk area if the endocardial mircrosphere flow was less than 0.25 ml/min/g. The normal region was defined by five transmural sectors located in the posterior lateral wall at the base of the heart (sectors 5, 6, 7 of the basal slice, and sectors 6 and 7 of the midbasal slice). In the normal territory, the average strains were radial 19.1% and circumferential -11.4%; this is in the same range as the values calculated for the MR-normal dogs. Differences were also observed between normal and risk-area territories; the interested reader is referred to [43] for the details.

12.6 Validation of results

The validation of LV motion and deformation results is an extremely important and often neglected aspect of the work in the general field of medical image analysis. In general, we need to address the following questions:

- Does the imaging modality produce an accurate picture of the underlying geometry and/or displacement and velocity?
- Does the analysis algorithm extract these data accurately and reliably?
- Are the results meaningful for clinical and/or physiological purposes? Do they discriminate between healthy/disfunctional regions?

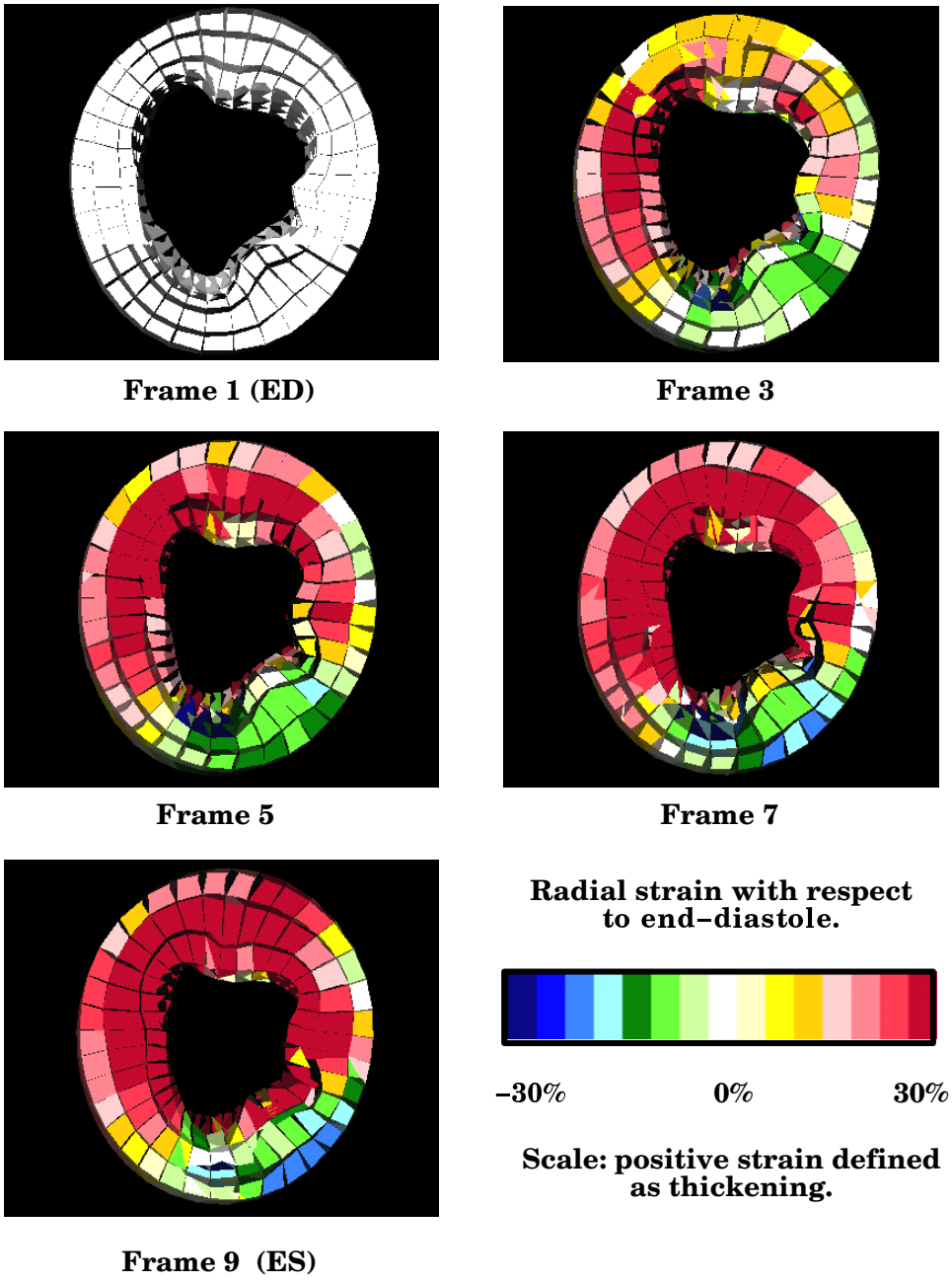

Figure 12.14: Radial strain development in a section of a postocclusion left ventricle, as estimated from MRI data. Note the infarct region on the right colored as blue-green. Compare the change from Fig. 12.12. (For a color version of this Figure see Plate 16 in the color section of this book.)

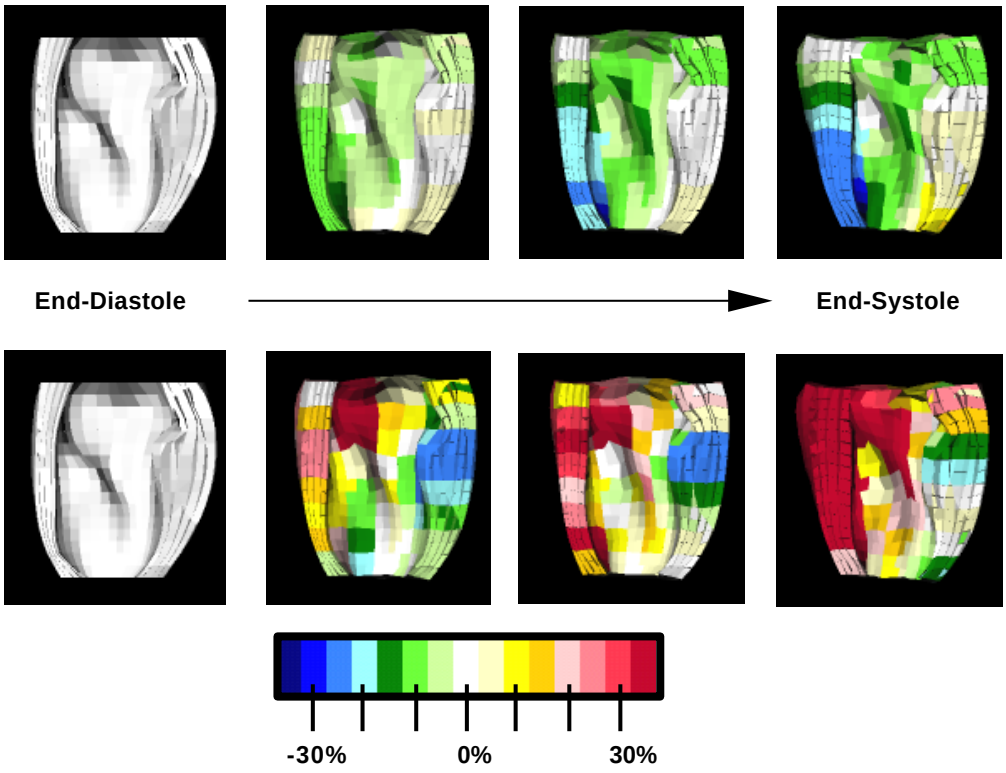

Figure 12.15: A long-axis cut-away sectional view of the left ventricle showing circumferential (top) and radial (bottom) % strain development in a dog, as derived from 3D ultrasound data, following left anterior descending coronary artery occlusion (on the lower right half of the heart). Note the normal behavior in the left half of the heart. There was positive radial strain (thickening) and negative circumferential strain (shortening) as we move from end diastole to end systole. The lower right half of the heart, where the affected region was located, showed almost the opposite behavior, as expected. (For a color version of this Figure see Plate 17 in the color section of this book.)

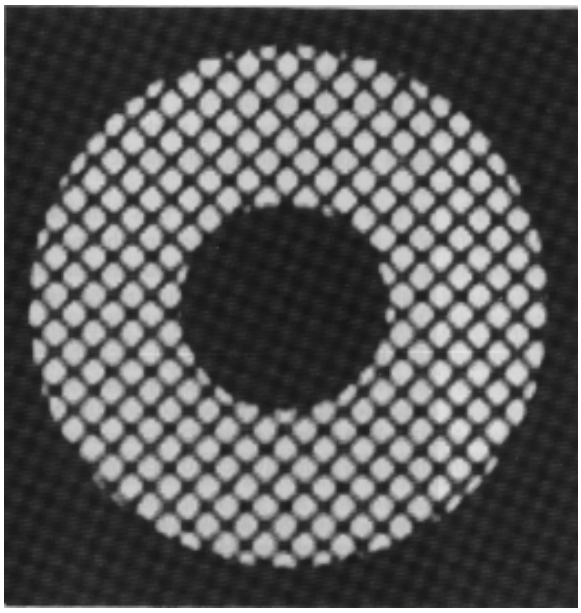

Figure 12.16: MR image of gel phantom with SPAMM (tag) stripes in undeformed state. From Kraitchman [62]. Courtesy of Leon Axel, University of Pennsylvania.

In general, the first two questions are difficult to address in vivo. Often, phantoms are used with known shapes and displacements, so there is ground truth information with which to compare any measurements (e.g., [34, 62]). An example of this is shown in Fig. 12.16. In Young [63], it was shown that, away from the free surfaces of the gel-phantom, a Rivlin-Mooney [51] analytic model accurately reproduced the 2D displacement of magnetic tags. This showed agreement between the theory (model) and the image-derived displacements. However, the real *in vivo* measurement of the beating heart usually presents additional complexities that introduce problems not usually accounted for in phantoms, such as full and complex 3D motion and fast blood flow through the ventricle. These can generate artifacts in the images and cause significant distortions.

The second question has been attacked in approaches based on MR tagging (e.g., [1, 14, 18]) using simulations. One example, shown in Fig. 12.17, uses a kinematic model of the left ventricular motion [64] within an MR tag image simulator [65] to generate synthetic images with known displacements. Comparison with manual extraction has often been used as the gold standard to validate the process of tag extraction, as in [62].

In the shape-tracking work of Shi [38], implanted markers are used as the gold standard. These markers are physically implanted in the myocardium before the imaging. An MR image of a heart with the implanted markers is shown in

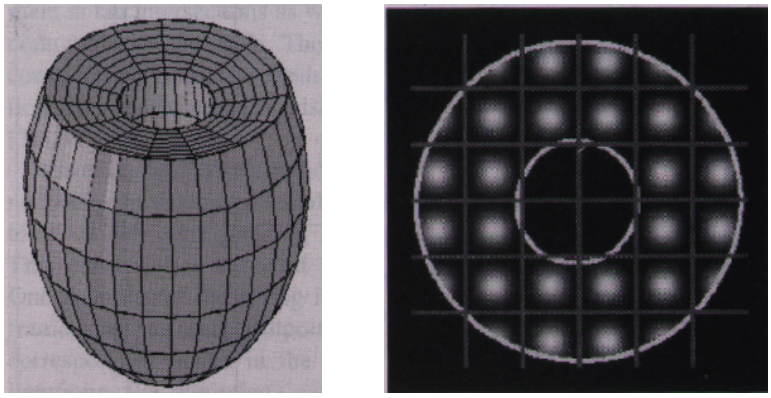

Figure 12.17: Example of the use of the cardiac simulator [64, 65] used to validate methods based on MR tagging. Left: the undeformed prolate spheroidal model of the LV in the reference state. Right: a tagged image corresponding to a selected image plane. From Amini [14]. Courtesy of Amir A. Amini, Washington University, St Louis.

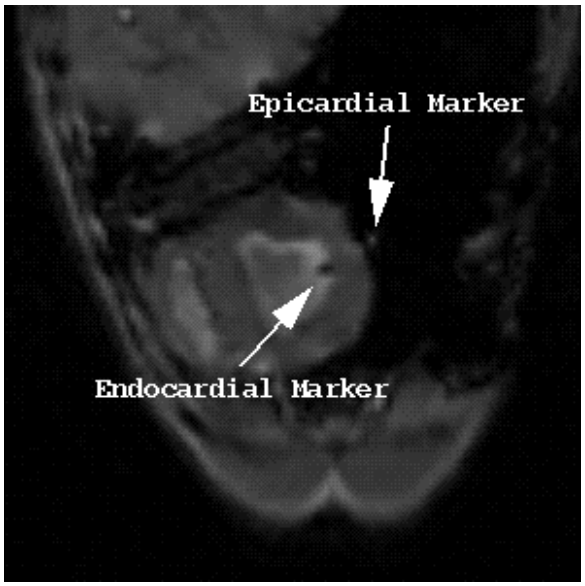

Figure 12.18: 2D MR image slice of left ventricle with implanted markers used to validate shape-based displacement estimates. From Shi [38].

Fig. 12.18. This approach to validation tries to attack the first two questions simultaneously. Here, algorithm-generated displacements are compared to the marker displacements (these are easily identifiable from the images). This technique has the disadvantage of comparing trajectories in a smaller number of points; however, it is done on *real* data, as opposed to simulations.

The third question is not addressed much in the image analysis literature, quantitatively. Often, an example of the results on a normal and a hypertrophic heart is shown and the differences "correlated" with other evidence from the cardiology literature. It is known from both work reported in the case study in this chapter (see Section 12.5) and from the work of Croisille et al. [60], that, on average, the changes between normal and abnormal regions in terms of radial and circumferential strains is on the order of 10–15 %, and much smaller in the case of borderline regions. A quick calculation shows that in the case of MR-tagging-based work, where the tags are typically 5 voxels apart at end-diastole, the change in the spacing at end-systole is going to be around 0.5 voxels or less. In the case of shape-based methods where the whole of the ventricle is used, this number is somewhat larger (around 0.8 voxels). If such changes are to be detected reliably, and we were to ignore accumulated tracking errors after the tags and/or boundaries have been extracted, we need to be able to extract tags/boundaries at a precision of 0.25–0.4 voxel or less. This is currently beyond the performance level of all automatic algorithms on real data; hence, manual and semiautomatic algorithms are used in most cases. In both the case study and [60], the reported results are averaged over a number of studies. This may be useful for exploring the physiology but not plausible for diagnosis, unless the results are averaged over large sections of the ventricle.

12.7 Conclusions and further research directions

The major problem/bottleneck in most of the work presented in this chapter is the extraction of features such as tag lines and especially left ventricular surfaces from the image data. As mentioned in the previous section, there is a reliance on manual and semiautomatic techniques to obtain this information. Another problem, which is less an issue of image analysis and more an issue of medical imaging technology, is the difficulty of using magnetic resonance in a clinical setting. It is not possible to image patients in an emergency room (as is the case for example with ultrasound), and metallic objects such as pacemakers cause serious problems and dangers when placed in the magnet.

As mentioned earlier, most of the models used to smooth and/or interpolate the displacement field are passive; they do not contain any active contraction information. This can result in an underestimation of the deformation, as the model biases the results toward no change. This was noted in the work of Park [48] and is the reason why no spatial smoothness was employed there. This, however, is not a sufficient solution to the problem, as some spatial smoothing is often needed to cope with the noise in the data and the sparseness in the image information. A possibly

better solution would be to incorporate some knowledge of the active contraction of the left ventricle during the first half of the cardiac cycle. This has the potential of eliminating the bias problem, although it would introduce more parameters to be set or ideally estimated from the image data.

Magnetic resonance represents a promising modality and the development of improved analysis techniques will enhance the possibilities of it being used clinically. In the meantime we note that improvements in 3D echo technology, such as the introduction of harmonic imaging [66] and contrast agents [67], are beginning to make this modality an attractive and somewhat cheaper alternative. Some preliminary work has been reported in the case study (see also [43].) However, segmenting ultrasound images is a very challenging problem whose solution will most likely require the use of temporal as well as spatial information. Some interesting feature-extraction work was reported in [68].

12.8 Appendix A: Comparison of mechanical models to regularization

In this appendix, we explicitly compare the internal energy function generated by isotropic linear elasticity with the equivalent energy function generated by the Horn and Schunk regularizer, as shown in Eq. (12.4).

Isotropic linear elasticity. The internal energy function generated by linear elasticity has the form:

$$W = e^t C e\,, \tag{12.15}$$

where e is the strain tensor written in vector form and C is the matrix of elastic properties. (See also Section 12.5.2 in the case study.) In the case of infinitesimal linear elasticity, the strain tensor ϵ is defined as

$$\epsilon_{ij} = \frac{1}{2}\left(\frac{\partial u_i}{\partial x_j} + \frac{\partial u_j}{\partial x_i}\right)\,. \tag{12.16}$$

The strain is the symmetric component of the displacement to position Jacobian. Since it is a symmetric 3×3 matrix, we can rewrite it in vector form as

$$e = [\epsilon_{11}, \epsilon_{22}, \epsilon_{33}, \epsilon_{12}, \epsilon_{13}, \epsilon_{33}]^t\,. \tag{12.17}$$

We can also define the complement tensor $theta$, which is the small rotation tensor, as the antisymmetric component of this Jacobian. Similarly, we write this in vector form as

$$\omega = [\theta_{11}, \theta_{22}, \theta_{33}, \theta_{12}, \theta_{13}, \theta_{33}]^t\,. \tag{12.18}$$

The principle of material frame indifference [51] states that the internal energy function must be invariant to rigid translation and rotation. A sufficient condition is that it must be a function of ϵ and not a function of ω.

Relation between regularization and linear elasticity. The internal energy function used by Horn and Schunk can be rewritten as

$$W_2 = (e + \omega)^t (e + \omega)\,. \tag{12.19}$$

This is a function of the small rotation vector and hence does not satisfy the principle of material frame indifference. So this "mechanical" model is unrealizable, which means that no material could exist with this strain energy function. This is because it contradicts the second law of thermodynamics, since the internal energy function is not a function of the deformation alone but also a function of the rotation ω. If the internal energy changes when a global rotation is applied, we arrive at the following problem: Suppose that work is needed to rotate the object clockwise. From conservation principles, this energy will be returned when the object is turned counter-clockwise. We can keep turning the object counter-clockwise to get more and more energy, and in this way we have created a *perpetual motion machine*.

Therefore, one could define all realizable mechanical models as the subset of regularization functionals that are invariant to global translation and rotation. Viewing the problem in this way does not make finding a model necessarily easier, but it does provide a way to eliminate inadmissible models.

12.9 References

[1] E. Haber, D. N. Metaxas, and L. Axel, "Motion analysis of the right ventricle from MRI images," in *In Medical Image Computing and Computer-Assisted Intervention -MICCAI*, (Cambridge, Mass.), October 1998.

[2] N. Gassler, H.-O. Wintzwer, H.-M. Stubbe, A. Wullbrand, and U. Helmchen, "Transmyocardial laser revascularization: histological features in hyman nonresponder myocardium," *Circulation*, pp. 371–5, 1997.

[3] K. Gallagher, G. Oksada, M. Miller, W. Kemper, and J. Ross, "Nonuniformity of inner and outer systolic wall thickening in conscious dogs," *Am J. Physiology*, vol. 249, pp. H241–H248, 1985.

[4] T. Freeman, J. Cherry, and G. Klassen, "Transmural myocardial deformation in the canine left ventricular wall," *Am J. Physiology*, vol. 235, pp. H523–H530, 1978.

[5] D. P. Dione, P. Shi, W. Smith, P. D. Man, J. Soares, J. S. Duncan, and A. J. Sinusas, "Three-dimensional regional left ventricular deformation from digital sonomicrometry," in *19th Annual International Conference of the IEEE Engineering in Medicine and Biology Society*, (Chicago, Ill.), pp. 848–851, March 1997.

[6] L. Waldman, Y. Fung, and J. Covell, "Transmural myocardial deformation in the canine left ventricle," *Circ Res*, vol. 57, pp. 152–163, 1985.

[7] G. D. Meier, M. Ziskin, W. P. Santamore, and A. Bove, "Kinematics of the beating heart," *IEEE Trans Biomed Eng*, vol. 27, pp. 319–329, 1980.

[8] N. Ingels, G. Daughters, E. Stinson, and E. Alderman, "Measurement of midwall myocardial dynamics in intact man by radiography of surgically implanted markers," *Circulation*, vol. 52, pp. 859–867, November 1975.

[9] J. M. Dieudonne, "Gradients de directions et la deformations principales dans la paroi ventriculaire gauch normale," *J. Physiol. Paris*, vol. 61, pp. 305–330, 1969.

[10] H. Azhari *et al.*, "Noninvasive quantification of principal strains in normal canine hearts using tagged MRI images in 3D," *Am. J. Physiol.*, vol. 264, pp. H205–H216, 1993.

[11] L. Axel, "Physics and technology of cardiovascular MR imaging," *Cardiology Clinics*, vol. 16, no. 2, pp. 125–133, 1998.

[12] B. K. P. Horn, *Robot Vision*. New York: McGraw-Hill, 1986.

[13] E. R. McVeigh, "Regional myocardial function," *Cardiology Clinics*, vol. 16, no. 2, pp. 189–206, 1998.

[14] A. A. Amini, Y. Chen, R. W. Curwen, V. Manu, and J. Sun, "Coupled b-snake grides and constrained thin-plate splines for analysis of 2-D tissue defomations from tagged MRI," *IEEE Transactions on Medical Imaging*, vol. 17, pp. 344–356, June 1998.

[15] W. S. Kerwin and J. L. Prince, "Cardiac material markers from tagged MR images," *Medical Image Analysis*, vol. 2, no. 4, pp. 339–353, 1998.

[16] A. A. Young, D. L. Kraitchman, L. Dougherty, and L. Axel, "Tracking and finite element analysis of stripe deformation in magnetic resonance tagging," *IEEE Transactions on Medical Imaging*, vol. 14, pp. 413–421, September 1995.

[17] T. S. Denney, Jr and J. L. Prince, "Reconstruction of 3-D Left Ventricular Motion from Planar Tagged Cardiac MR Images: An Estimation Theoretic Approach," *IEEE Transactions on Medical Imaging*, vol. 14, pp. 625–635, December 1995.

[18] J. L. Prince and E. R. McVeigh, "Motion estimation from tagged MR image sequences," *IEEE Transactions on Medical Imaging*, vol. 11, pp. 238–249, June 1992.

[19] S. N. Gupta and J. L. Prince, "On variable brightness optical flow for tagged MRI," in *Information Processing in Medical Imaging*, June 1995.

[20] M. Guttman, J. Prince, and E. McVeigh, "Tag and contour detection in tagged MR images of the left ventricle," *IEEE Transactions on Medical Imaging*, vol. 13, no. 1, pp. 74–88, 1994.

[21] S. Kumar and D. Goldgof, "Automatic tracking of SPAMM grid and the estimation of deformation parameters from cardiac images," *IEEE Transactions on Medical Imaging*, vol. 13, March 1994.

[22] T. S. Denney Jr, "Estimation and detection of myocardial tags in MR images without user-defined myocardial contours," *IEEE Transactions on Medical Imaging*, vol. 18, pp. 330–344, April 1999.

[23] M. Kass, A. Witkin, and D. Terzopoulos, "Snakes: Active contour models," in *Proc. Int. Conf. on Computer Vision*, pp. 259–268, 1987.

[24] T. McInerney and D. Terzopoulos, "Deformable models in medical image analysis: a survey," *Medical Image Analysis*, vol. 1, no. 2, pp. 91–108, 1996.

[25] A. A. Amini, R. W. Curwen, R. T. Constable, and J. C. Gore, "MR physics-based snake tracking and dense deformations from tagged cardiac images," in *AAAI Int. Symp. Comp. Vision Med. Image Processing.*, 1994.

[26] S. Androutsellis-Theotokis and J. L. Prince, "Experiments in multiresolution motion estimation for multifrequency tagged cardiac MR images," in *Int. Conf. on Image Processing*, (Lausanne, Switzerland), September 1996.

[27] P. van Dijk, "Direct cardiac NMR imaging of heart wall and blood flow velocity," *J. Comp. Assist. Tomog.*, vol. 8, pp. 429–436, 1984.

[28] G. Nayler, N. Firmin, and D. Longmore, "Blood flow imaging by cine magnetic resonance," *J. Comp. Assist. Tomog.*, vol. 10, pp. 715–722, 1986.

[29] N. J. Pelc, "Myocardial motion analysis with phase contrast cine MRI," in *Proceedings of the 10th Annual SMRM*, (San Francisco), p. 17, 1991.

[30] N. J. Pelc, R. Herfkens, and L. Pelc, "3D analysis of myocardial motion and deformation with phase contrast cine MRI," in *Proceedings of the 11th Annual SMRM*, (Berlin), p. 18, 1992.

[31] N. Pelc, R. Herfkens, A. Shimakawa, and D. Enzmann, "Phase contrast cine magnetic resonance imaging," *Magn. Res. Quart.*, vol. 7, no. 4, pp. 229–254, 1991.

[32] V. Wedeen, "Magnetic Resonance Imaging of Myocardial Kinematics: Technique to Detect, Localize and Quantify the Strain Rates of Active Human Myocardium," *Magn. Reson. Med.*, vol. 27, pp. 52–67, 1992.

[33] F. G. Meyer, R. T. Constable, A. J. Sinusas, and J. S. Duncan, "Tracking Myocardial Deformation Using Phase Contrast MR Velocity Fields: A Stochastic Approach," *IEEE Transactions on Medical Imaging*, vol. 15, August 1996.

[34] T. Constable, K. Rath, A. Sinusas, and J. Gore, "Development and evaluation of tracking algorithms for cardiac wall motion analysis using phase velocity MR imaging," *Magn. Reson. Med.*, vol. 32, pp. 33–42, 1994.

[35] Y. Zhu, M. Drangove, and N. J. Pelc, "Estimation of deformation gradient and strain from cine-pc velocity data," *IEEE Transactions on Medical Imaging*, vol. 16, December 1997.

[36] R. Herfkens, N. Pelc, L. Pelc, and J. Sayre, "Right ventricular strain measured by phase contrast MRI," in *Proceedings of the 10th Annual SMRM*, (San Francisco), p. 163, 1991.

[37] P. Shi, A. J. Sinusas, R. T. Constable, and J. S. Duncan, "Volumetric Deformation Analysis Using Mechanics-Based Data Fusion: Applications in Cardiac Motion Recovery," *International Journal of Computer Vision, Kluwer*, in-press.

[38] P. Shi, A. J. Sinusas, R. T. Constable, E. Ritman, and J. S. Duncan, "Point-tracked quantitative analysis of left ventricular motion from 3D image sequences," *IEEE Transactions on Medical Imaging*, in-press.

[39] C. Kambhamettu and D. Goldgof, "Curvature-based approach to point correspondence recovery in conformal nonrigid motion," *CVGIP: Image Understanding*, vol. 60, pp. 26–43, July 1994.

[40] I. Cohen, N. Ayache, and P. Sulger, "Tracking points on deformable objects using curvature information," in *Lecture Notes in Computer Science-ECCV92*, pp. 458–466, Springer Verlag, 1992.

[41] J. McEachen, A. Nehorai, and J. Duncan, "A recursive filter for temporal analysis of cardiac function," in *IEEE Workshop on Biomedical Image Analysis*, (Seattle), pp. 124–133, June 1994.

[42] H. D. Tagare, "Shape-based nonrigid curve correspondence with application to heart motion analysis," *IEEE Transactions on Medical Imaging*, vol. 18, pp. 570–579, July 1999.

[43] X. Papademetris, A. J. Sinusas, D. P. Dione, and J. Duncan, "3D cardiac deformation from ultrasound images," in *Medical Image Computing and Computer Aided Intervention (MICCAI)*, (Cambridge, England), pp. 420–429, September 1999.

[44] S. Song and R. Leahy, "Computation of 3D velocity fields from 3D cine CT images," *IEEE Transactions on Medical Imaging*, vol. 10, pp. 295–306, Sept 1991.

[45] A. A. Young, "Model tags; direct 3D tracking of heart wall motion from tagged MRI images," in *MICCAI*, (Boston, Massachusetts), pp. 92–101, October 1998.

[46] X. Papademetris, P. Shi, D. P. Dione, A. J. Sinusas, and J. S. Duncan, "Recovery of soft tissue object deformation using biomechanical models," in *Information Processing in Medical Imaging*, (Visegrad, Hungary), pp. 352–357, June 1999.

[47] W. Odell, C. Moore, and E. McVeigh, "Displacement field fitting approach to calculate 3D deformations from parallel tagged grids," *J. Mag. Res. Imag.*, vol. 3, p. P208, 1993.

[48] J. Park, D. N. Metaxas, and L. Axel, "Analysis of left ventricular wall motion based on volumetric deformable models and MRI-SPAMM," *Medical Image Analysis*, vol. 1, no. 1, pp. 53–71, 1996.

[49] B. K. P. Horn and B. G. Schunk, "Determining optical flow," *Artificial Intelligence*, vol. 17, pp. 185–203, 1981.

[50] P. J. Hunter, A. McCulloch, and P. Nielsen, eds., *Theory of Heart*. Berlin: Springer-Verlag, 1991.

[51] L. E. Malvern, *Introduction to the Mechanics of a Continuous Medium*. Englewood Cliffs, New Jersey: Prentice-Hall, 1969.

[52] K. Bathe, *Finite Element Procedures in Engineering Analysis*. New Jersey: Prentice-Hall, 1982.

[53] D. Terzopoulos and D. Metaxas, "Dynamic 3D models with local and global deformation: deformable superquadrics," *IEEE Transactions on Pattern Analysis and Machine Intelligence*, vol. 13, no. 17, 1991.

[54] B. Horowitz and S. Pentland, "Recovery of non-rigid motion and structure," in *Proceedings of the IEEE Conference on Computer Vision and Pattern Recognition*, (Maui), pp. 325–330, June 1991.

[55] C. Nastar and N. Ayache, "Classification of nonrigid motion in 3D images using physics-based vibration analysis," in *Workshop on Biomedical Image Analysis*, (Seattle, Washington), pp. 61–69, 1994.

[56] X. Papademetris, J. V. Rambo, D. P. Dione, A. J. Sinusas, and J. S. Duncan, "Visually interactive cine-3D segmentation of cardiac MR images," *Suppl. to the J. Am. Coll. of Cardiology*, vol. 31, February 1998.

[57] A. Chakraborty, M. Worring, and J. S. Duncan, "On multi-feature integration for deformable boundary finding," *Proc. Int. Conf. on Computer Vision*, pp. 846–851, 1995.

[58] J. M. Guccione and A. D. McCulloch, "Finite element modeling of ventricular mechanics," in *Theory of Heart* (P. J. Hunter, A. McCulloch, and P. Nielsen, eds.), pp. 122–144, Berlin: Springer-Verlag, 1991.

[59] G. E. Christensen, R. D. Rabbitt, and M. I. Miller, "3D brain mapping using deformable neuroanatomy," *Physics in Medicine and Biology*, vol. 39, pp. 609–618, 1994.

[60] P. Croissile, C. C. Moore, R. M. Judd., J. A. C. Lima, M. Arai, E. R. McVeigh, L. C. Becker, and E. A. Zerhouni, "Differentiation of viable and nonviable myocardium by the use of three-dimensional tagged MRI in 2-day-old reperfused infarcts.," *Circulation*, vol. 99, pp. 284–291, 1999.

[61] A. J. Sinusas, K. A. Trautman, J. D. Bergin, D. D. Watson, M. Ruiz, W. H. Smith, and G. A. Beller, "Quantification of area of risk during coronary occlusion and degree of myocardial salvage after reperfusion with technetium-99m methoxyisobutyl isonitrile.," *Circulation*, vol. 82, pp. 1424–37, 1990.

[62] D. L. Kraitchman, A. A. Young, C. C, and L. Axel, "Semi-automatic tracking of myocardial motion in MR tagged images," *IEEE Transactions on Medical Imaging*, vol. 14, pp. 422–433, September 1995.

[63] A. A. Young, L. Axel, *et al.*, "Validation of tagging with MR imaging to estimate material deformation," *Radiology*, vol. 188, pp. 101–108, 1993.

[64] T. Arts, W. Hunter, A. Douglas, A. Muijtens, and R. Reneman, "Description of the deformation of the left ventricle by a kinematic model," *J. Biomechanics*, vol. 25, no. 10, pp. 1119–1127, 1992.

[65] E. Waks, J. L. Prince, and A. Douglas, "Cardiac motion simulator for tagged MRI," in *Mathematical Methods in Biomedical Imaging Analysis*, pp. 182–191, 1996.

[66] K. Caidahl, E. Kazzam, J. Lingberg, G. N. Andersen, J. Nordanstig, S. R. Dahlqvist, A. Waldenstro, and R. Wikh, "New concept in echocardiography: harmonic imaging of tissue withoug use of contrast agent.," *The Lancet*, vol. 352, pp. 1264–1270, 1999.

[67] T. R. Porter, F. Xie, A. Kricsfeld, A. Chiou, and A. Dabestani, "Improved endocardial border resolution using dobutamin stress endocardiography with intravenous sonicated dextrose albumin.," *J. Am College of Cardiology*, vol. 23, pp. 1440–43, 1994.

[68] M. M.-P. Miguel and J. A. Noble, "2D+T acoustic boundary detection in echocardiography," in *MICCAI*, (Boston, Massachusetts), October 1998.